ADVANCED MATERIALS
www.advmat.de

Heteroepitaxial Growth of B_5-Site-Rich Ru Nanoparticles Guided by Hexagonal Boron Nitride for Low-Temperature Ammonia Dehydrogenation

Sungsu Kang, Junyoung Cha, Young Suk Jo, Yu-Jin Lee, Hyuntae Sohn, Younhwa Kim, Chyan Kyung Song, Yongmin Kim, Dong-Hee Lim, Jungwon Park, and Chang Won Yoon**

Ruthenium is one of the most active catalysts for ammonia dehydrogenation and is essential for the use of ammonia as a hydrogen storage material. The B_5-type site on the surface of ruthenium is expected to exhibit the highest catalytic activity for ammonia dehydrogenation, but the number of these sites is typically low. Here, a B_5-site-rich ruthenium catalyst is synthesized by exploiting the crystal symmetry of a hexagonal boron nitride support. In the prepared ruthenium catalyst, ruthenium nanoparticles are formed epitaxially on hexagonal boron nitride sheets with hexagonal planar morphologies, in which the B_5 sites predominate along the nanoparticle edges. By activating the catalyst under the reaction condition, the population of B_5 sites further increases as the facets of the ruthenium nanoparticles develop. The electron density of the Ru nanoparticles also increases during catalyst activation. The synthesized catalyst shows superior catalytic activity for ammonia dehydrogenation compared to previously reported catalysts. This work demonstrates that morphology control of a catalyst via support-driven heteroepitaxy can be exploited for synthesizing highly active heterogeneous catalysts with tailored atomic structures.

1. Introduction

Ammonia has received significant attention as a promising hydrogen carrier for regularizing renewable energy utilization to achieve carbon neutrality. Owing to its high energy density, ease of liquefaction, and well-established transportation infrastructure, the use of ammonia as a hydrogen carrier can potentially overcome the temporal and geographical imbalance between the supply and demand for renewable energy.[1–4] Specifically, CO_2-free hydrogen produced using renewable energy is converted into ammonia, which is then shipped to a desired site using existing transport infrastructure. Finally, the hydrogen stored in the delivered ammonia is extracted through a chemical reaction and then used for energy generation in conjunction with fuel cells and H_2 turbines. Because mass production, storage, and transportation of ammonia are currently commercialized, ammonia dehydrogenation is the key process for completing the ammonia-based clean energy production–utilization cycle; thus, developing highly active and durable catalysts for ammonia dehydrogenation is necessary.

The ammonia dehydrogenation process is a multistep reaction comprising NH_3 adsorption, three N—H bond cleavage

S. Kang, Y. Kim, C. K. Song, J. Park
School of Chemical and Biological Engineering
Institute of Chemical Processes
Seoul National University
Seoul 08826, Republic of Korea
E-mail: jungwonpark@snu.ac.kr

S. Kang, Y. Kim, C. K. Song, J. Park
Center for Nanoparticle Research
Institute for Basic Science (IBS)
Seoul 08826, Republic of Korea

J. Cha, Y. S. Jo, Y.-J. Lee, H. Sohn, Y. Kim
Center for Hydrogen and Fuel Cell Research
Korea Institute of Science and Technology (KIST)
Seoul 02792, Republic of Korea

D.-H. Lim
Department of Environmental Engineering
Chungbuk National University
Chungbuk 28644, Republic of Korea

The ORCID identification number(s) for the author(s) of this article can be found under https://doi.org/10.1002/adma.202203364.

DOI: 10.1002/adma.202203364

J. Park
Institute of Engineering Research
College of Engineering
Seoul National University
Seoul 08826, Republic of Korea

J. Park
Advanced Institute of Convergence Technology
Seoul National University
Suwon 16229, Republic of Korea

C. W. Yoon
Hydrogen and Low Carbon Research Laboratories
Research Institute of Industrial Science and Technology (RIST)
Pohang 37673, Republic of Korea

C. W. Yoon
Hydrogen and Low Carbon Energy R&D Laboratories
POSCO N.EX.T Hub
Seoul 06194, Republic of Korea

C. W. Yoon
Department of Chemical Engineering
Pohang University of Science and Technology (POSTECH)
Pohang 37673, Republic of Korea
E-mail: cwyoon@postech.ac.kr

steps, H_2 desorption, and N_2 desorption. The nitrogen desorption step is regarded as the rate-determining step for ammonia dehydrogenation at low temperature, owing to the strong binding energy of nitrogen on metals (450–650 kJ mol^{-1}).[5–7] In this regard, extensive effort has been dedicated to lowering the kinetic barrier associated with the nitrogen desorption reaction.[8,9] As one strategy to promote N_2 desorption, Ru metal is employed as a monometallic active site because Ru has a suitable nitrogen binding energy.[6] Among different surfaces of Ru nanoparticles, the B_5-type step site, a step on the (001) surface of hexagonal close-packed (hcp) Ru, is known to exhibit the lowest activation energy for the N_2 desorption reaction and thus the highest activity for ammonia decomposition at low temperatures.[10–14] This property of the B_5 site is attributed to the pentagonal atomic arrangement of the five Ru atoms composing a step site,[10,15] and the unique structural feature of the B_5 site allows the favorable electronic and geometric properties for ammonia dehydrogenation.[16] On the other hand, the typical active sites of Ru catalysts consist mostly of thermodynamically stable (111) and quasi-planar (101) surfaces, simultaneously with other Ru surfaces distributed randomly.[10] In this situation, the population of B_5 sites is usually marginal because of the difficulties in selectively producing atomic steps on the Ru(001) surface.[17] Moreover, the density of B_5 sites is limitedly controlled by tuning the sizes of the nanoparticles depending on their morphology,[18–20] and Ru surfaces that are less active for N_2 desorption still exist considerably. Therefore, to design highly active ammonia dehydrogenation catalysts for low-temperature operation, new synthesis strategies that can selectively enhance the density of surface-exposed B_5 sites on Ru nanoparticles are required.

Herein, we introduce a novel synthesis using selective morphology-control driven by nanoscale heteroepitaxy. Ru nanoparticle catalysts with abundant B_5 sites are successfully synthesized on an atomically clean hexagonal boron nitride (h-BN) surface, which is ideal for low-temperature ammonia dehydrogenation. The hexagonal crystal symmetry of h-BN, identical to that of Ru, enables the epitaxial growth of hexagon-shaped Ru nanoparticles on the (001) surface as an inverse analogy to monolayer h-BN synthesized on Ru(001).[21] By activating the Ru/h-BN catalyst under the reaction condition, the B_5-site-rich Ru nanoparticles develop into a sharply faceted hexagonal morphology, which further increases the density of B_5 sites. Additionally, activation of the Ru/h-BN catalyst increases the electron density of the Ru metal. The resulting B_5-site-rich Ru/h-BN catalyst exhibits the highest activity for ammonia dehydrogenation among the Ru-based catalysts reported previously. Our work demonstrates that morphology control of a supported catalyst via heteroepitaxy from the catalyst support can be an effective strategy for synthesizing highly active, heterogeneous catalysts with desired structures.

2. Results and Discussion

2.1. Epitaxial Growth of B_5-Site-Rich Ru Nanoparticles on h-BN

h-BN sheets are chosen as the catalyst support to exploit the hexagonal symmetry of the h-BN(001) surface as a route to facilitate the formation of Ru B_5 sites on the widely exposed surface of the (001) crystal plane. This is beneficial for synthesizing B_5-site-rich Ru catalysts because the density of the B_5 sites increases with the exposed area of Ru(001).[10,11,22] This strategy is supported by the fact that the growth of monolayer h-BN is promoted by the Ru(001) surface.[21] The procedure for preparing the Ru/h-BN catalysts is summarized in **Figure 1**a. Ru (1 wt%) is loaded on h-BN sheets by the incipient wetness impregnation (IWI) method, in which $Ru_3(CO)_{12}$ dissolved in acetone was used as a precursor (see the Experimental Section for details). Despite the low surface area, pore volume, and acidic-basic sites of the h-BN sheets compared to other supports, nanometer-sized hcp Ru particles are uniformly synthesized on the h-BN sheets (Table S1 and Figures S1–S4, Supporting Information). The h-BN sheets have wide faces, corresponding to the (001) surface of h-BN, which are a few micrometers in width, as shown in Figure S5 (Supporting Information).

The transmission electron microscopy (TEM) image of a representative Ru/h-BN catalyst particle is shown in Figure 1b and Figure S6 (Supporting Information) to demonstrate the overall morphology. Many of the Ru nanoparticles, which appear as dark contrast in the TEM image, are located on the face of the h-BN sheet on the h-BN(001) surface. The Ru nanoparticles of the Ru/h-BN catalyst have a slightly different shape, but most of them are hexagonal with rounded corners and are ≈10 nm in size. The high-resolution TEM image (Figure 1c), obtained along the h-BN[001] zone axis, shows the formation of Ru nanoparticles along the hexagonal lattices of h-BN. Owing to the observed interference between the lattice of the Ru nanoparticles and the lattice of h-BN, long-range hexagonal patterns, known as Moiré patterns, are visible on the Ru nanoparticles. The hexagonal Moiré patterns are typically observed when two types of hexagonal lattices are rotated and superimposed on each other, indicating that the Ru nanoparticles are oriented along the [001] zone axis.[23,24] The fast Fourier-transform (FFT) patterns of the regions with Ru nanoparticles, indicated by orange boxes in Figure 1c, confirm the [001] zone axis orientation of the synthesized Ru nanoparticles on the (001) surface of h-BN (Figure 1d). The FFT patterns show peaks originating from the Ru nanoparticles and h-BN sheet, which are highlighted with orange circles and dotted lines in Figure 1d, respectively. The epitaxial relationship between the Ru nanoparticles and h-BN sheet can be further supported by constructing atomistic models, where the hexagonal Moiré patterns are well reproduced (Figure 1e).

The high-angle annular dark-field (HAADF) scanning TEM (STEM) image of an epitaxial Ru nanoparticle on the h-BN sheet in Figure 1f clearly shows the elongated hexagonal shape of the Ru nanoparticle with round edges in atomic resolution. A HAADF-STEM image of the underlying h-BN obtained at a different focus is presented in Figure S7 (Supporting Information). The long edges of the Ru nanoparticles are atomically sharp Ru{100} planes, and the other straight edges also belong to Ru{100}. Importantly, changes in the image contrast of the Ru atomic columns, which depend on the number of atoms along the projection column, reflect the arrangement of Ru atoms at the B_5 sites, as presented in the atomistic model in Figure 1f.

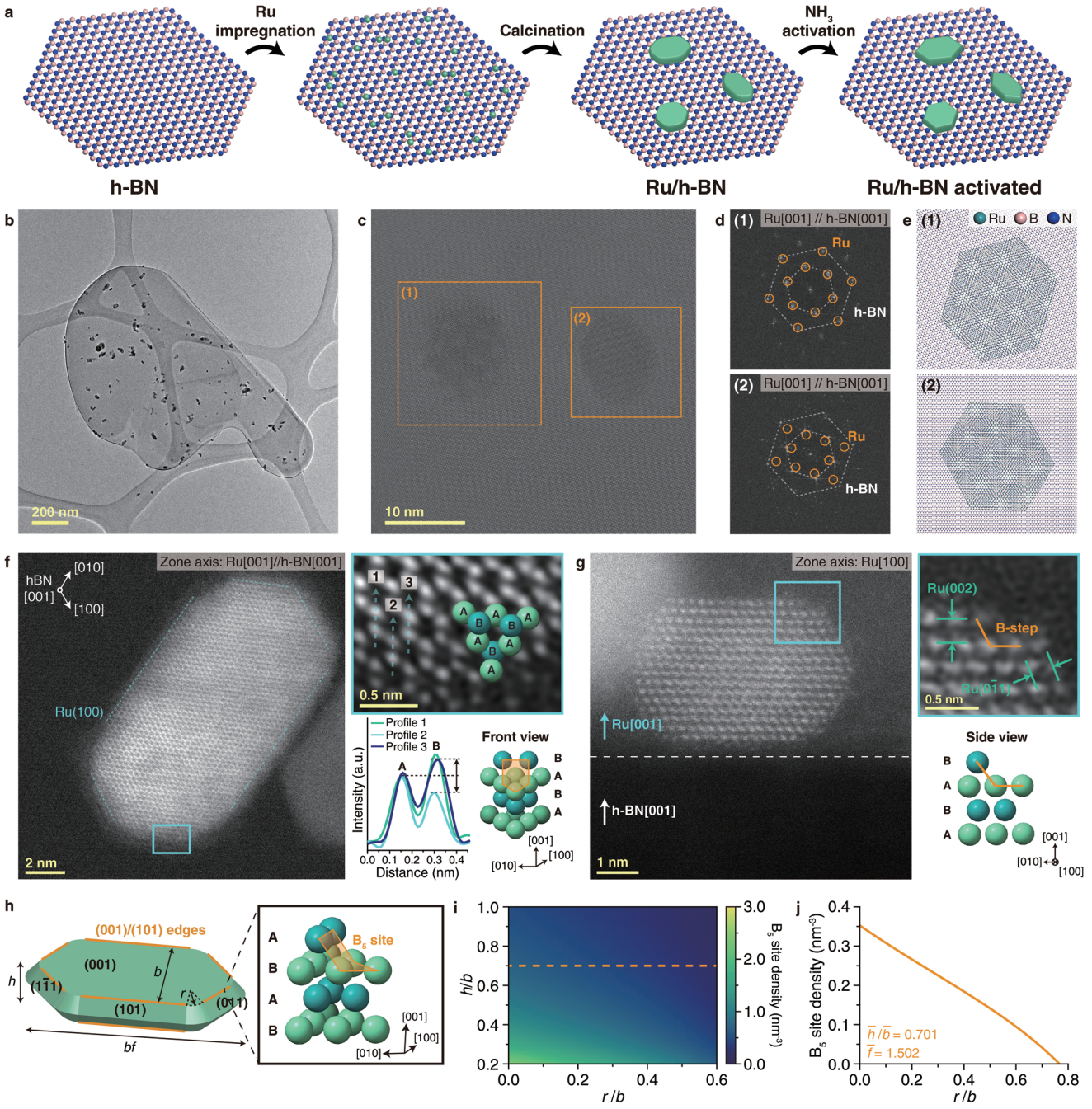

Figure 1. Preparation and structural characterization of Ru/h-BN catalyst. a) Schematic of preparation of Ru/h-BN catalyst. b) TEM image of synthesized Ru/h-BN catalyst. c) High-resolution TEM image of Ru nanoparticles supported on h-BN. d) Fast Fourier-transforms of boxed regions shown in (c). The hexagonal patterns from Ru{100} and h-BN{100} lattices are marked with circles and dotted lines, respectively. e) Atomistic models of Ru/h-BN observed in (c). f) HAADF-STEM image of Ru/h-BN and B_5 site, viewed in [001] direction of h-BN and Ru. The left panel shows the entire shape of the Ru nanoparticle. The straight (100) edges of the Ru nanoparticle are marked with dotted lines. The top-right panel shows low-pass filtered, magnified image of the boxed region in the left panel. The bottom-right panel shows intensity profiles along the lines presented in the top-right panel. The stronger contrast at location B in profiles 1 and 3 indicates the presence of step sites at the Ru nanoparticle edge as depicted in the atomistic model. g) Cross-sectional HAADF-STEM image of Ru/h-BN (left). The top-right panel shows low-pass filtered, magnified image of the boxed region in the left panel. The bottom-right panel shows atomistic model of the B_5 site observed in the top-right panel. h) Schematic of the model Ru nanoparticle used for B_5 site density estimation (Supporting Information). Locations where B_5 sites can exist are marked with orange lines. The inset shows atomic model of B_5 site. i) Dependence of B_5 site density on the height and radius of curvature in the model Ru nanoparticle. j) B_5 site density as a function of radius of curvature in an average Ru nanoparticle observed in our analyses. The result corresponds to the dotted line marked in (i).

The presence of B_5 sites on the Ru nanoparticles in the Ru/h-BN catalyst is further confirmed by cross-sectional HAADF-STEM imaging (Figure 1g and Experimental Section), from which the 3D morphology of the Ru nanoparticles can be predicted. The morphology of the cross-sectional Ru/h-BN sample is shown in Figure S8 (Supporting Information). The atomically resolved cross-sectional HAADF-STEM image indicates that the observed Ru nanoparticles supported on the h-BN(001) surface have well-defined surface facets composed of mostly (001) and (100) planes. Consequently, the combined plane-view and cross-sectional observations of Ru/h-BN indicate that the Ru nanoparticles are mostly terminated with {001} and {101} surfaces and have a hexagonal bifrustum shape with rounded bases, as illustrated in Figure 1h and Figure S9 (Supporting Information). In addition, an atomic step, identified to be a B_5 site, is located on the (001) plane. Additional cross-sectional STEM images showing the presence of steps at the (001)/(101) edges of the Ru nanoparticles are provided in Figure S10 (Supporting Information).

Modeling the morphology of the Ru nanoparticles indicates that the morphology of the optimal Ru nanoparticle with the highest B_5 sites density is close to that of the Ru nanoparticles prepared on h-BN. For the Ru nanoparticle with a hexagonal prism morphology and a rounded base, the shape of the nanoparticle can be described by the height h, length of the minor axis b, ratio of the major to minor axis f, and radius of curvature of the rounded edge r of the nanoparticle. Considering that one B_5 site presents every 0.275 nm along the (001)/(101) edge, the number of B_5 sites per unit Ru volume increases as h and r/b decrease, as presented in Figure 1i (details are provided in the Supporting Information and Figure S11, Supporting Information). In other words, the more planar the shape and sharper the corners of the hexagonal Ru nanoparticles, the higher the density of the B_5 sites. We also calculate the B_5 site density as a function of r/b in Figure 1j for an average Ru nanoparticle whose mean shape parameters are determined to be $\overline{h}$ = 5.62 nm, $\overline{b}$ = 8.02 nm, and $\overline{f}$ = 1.50 from multiple plan-view and cross-sectional (S)TEM images (for example, Figures S6 and S10, Supporting Information). The calculated B_5 site density might be overestimated because of the potential heterogeneity of the local surface structure as well as nanoparticle sizes. Nevertheless, the results indicate that a hexagonal planar-shaped Ru particle with a low height and sharp corners is likely favorable for ammonia dehydrogenation because of the abundance of B_5 sites. Compared to the slightly rounded Ru nanoparticles, the well-developed hexagonal Ru nanoparticles exhibit improved catalytic activity due to the increased density of B_5 sites (see **Figure 2**).

To understand how the h-BN support affects the structure of the Ru active sites, the products from each step of the Ru/h-BN catalyst synthesis are examined. After the impregnation step, small Ru clusters are formed and localized to the edges of the h-BN sheet (Figure S12, Supporting Information) because of the interactions between the negatively charged h-BN edges and ionic Ru clusters.[25] Next, air calcination leads to the formation of elongated hexagonally shaped RuO_2 nanoparticles on the face side of the h-BN sheets by providing thermal energy to mobilize the Ru clusters (Figure S13, Supporting Information).[26] The RuO_2 nanoparticles are gradually reduced by supplying 75%H_2/N_2 mixture gas at 450 °C, resulting in the formation of elongated hexagonal Ru(0) nanoparticles grown epitaxially on the hexagonal h-BN surface as characterized by high-resolution TEM (Figure 1). The elongated hexagonal morphology and the epitaxial relationship of the Ru nanoparticles increase the exposure of the Ru(101)/(001) edge,[27] ultimately increasing the B_5 sites. On the other hand, when a Ru/h-BN catalyst is prepared by vacuum calcination followed by reduction to bypass the RuO_2 formation, epitaxially grown Ru(0) nanoparticles with chain-like morphology are formed (Figure S14, Supporting Information), indicating that the epitaxy is driven by h-BN surface.

Ru catalysts are prepared on an γ-alumina (Al_2O_3) support with a cubic spinel structure and a silica (SiO_2) support with an amorphous structure to further examine the effects of support crystal structure (Experimental Section, Table S1, and Figures S3 and S15, Supporting Information). Interestingly, the high-resolution TEM images of Ru/Al_2O_3 and Ru/SiO_2 show that most of the Ru nanoparticles are irregularly shaped and are randomly placed on the Al_2O_3 and SiO_2 supports (Figure S16, Supporting Information). These results indicate the absence of specific interactions between Ru and the supports, presumably because of differences in their crystal structures and lattice spacings. On the other hand, the identical symmetry of Ru(001) and h-BN(001) induces the formation of a stable Ru–support interface, as the small lattice mismatch between the (100) lattice spacings of Ru (2.75 Å) and h-BN (2.50 Å) generates little interfacial strain.[28,29] Similar situations, in which the structure of a crystal is guided by the atomic arrangement of the underlying substrate, are often observed. Many 2D materials, including h-BN, have been synthesized on substrates with the same symmetry and similar lattice parameters,[30] and one specific phase of Rh_2O_3 nanocrystals has been synthesized on h-BN(001) with its lattice aligned to the h-BN lattice.[31] Accordingly, atomically clean surfaces with hexagonal lattice structure such as highly ordered pyrolytic graphite will induce the formation of epitaxial Ru nanoparticles.[27] Nonetheless, the use of h-BN as a support provides an additional advantage. Because high temperatures are generally required to make rearrangement of Ru metals for the formation of hexagon-shaped nanoparticles, the high thermal stability of h-BN is helpful. Additionally, high chemical stability of h-BN allows various chemical treatment to produce Ru NPs with desired Ru sizes.

2.2. Activation of Ru/h-BN Catalyst

The prepared Ru/h-BN catalyst is utilized for ammonia dehydrogenation at a gas hourly space velocity (GHSV) of 60 000 $mL_{NH_3}\ g_{cat}^{-1}\ h^{-1}$ and a temperature of 450 °C. For comparison, the Ru/Al_2O_3 and Ru/SiO_2 catalysts are also tested for ammonia dehydrogenation under the identical condition. The catalytic activity of Ru/h-BN increases rapidly during the first few hours of the reaction and continues to increase gradually at a slower rate, finally reaching a maximum value after 30 h of the reaction (Figure 2a). On the other hand, the catalytic activity of Ru/Al_2O_3 and Ru/SiO_2 decreases with the reaction time. Note that the activity of Ru/h-BN is higher than that of Ru/Al_2O_3 and Ru/SiO_2 despite the low surface area of Ru/h-BN (Table S1,

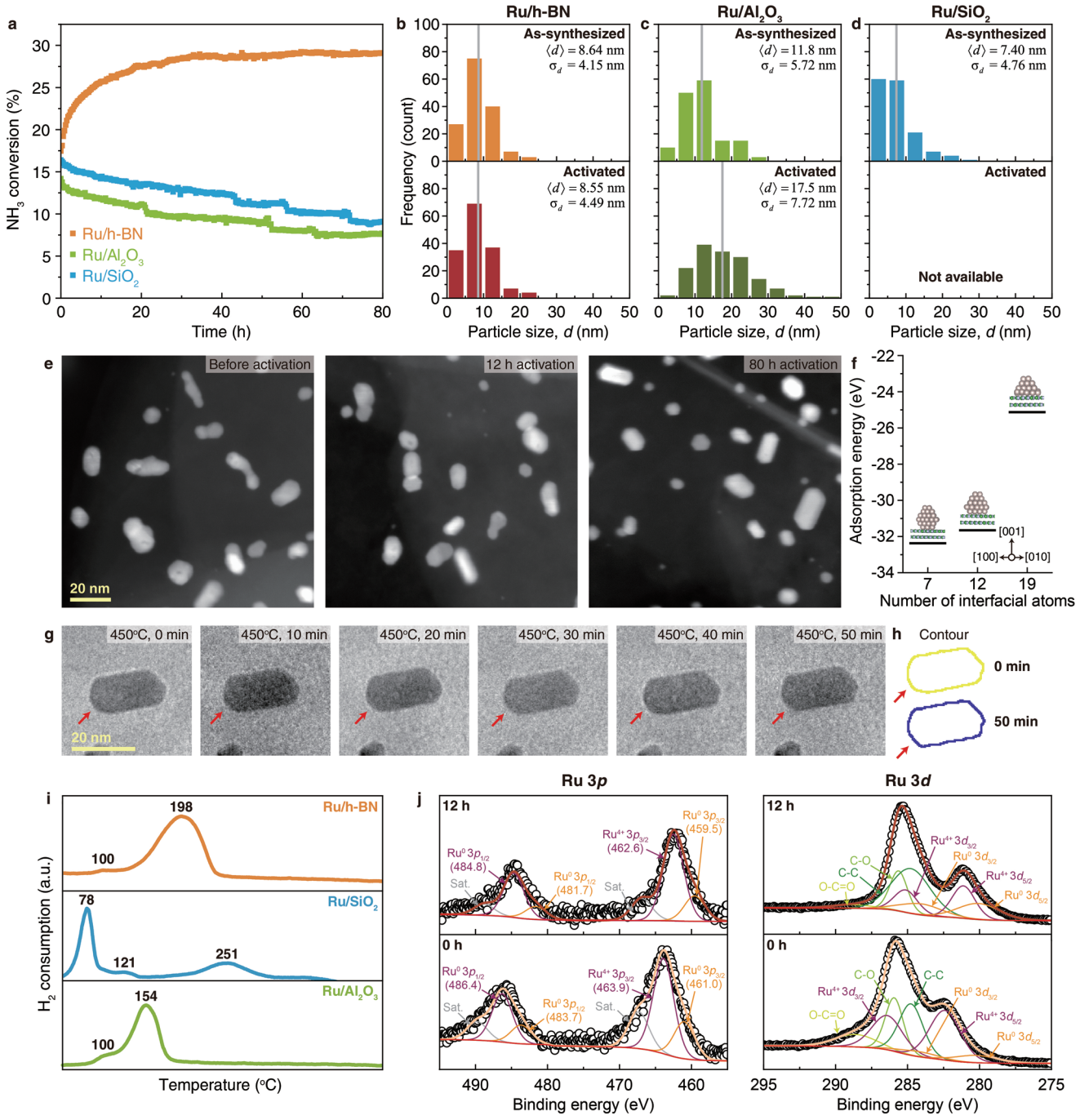

Figure 2. Activation of Ru/h-BN catalyst under reaction conditions. a) Comparison of stability of Ru/h-BN, Ru/Al_2O_3, and Ru/SiO_2 catalysts for ammonia decomposition at a GHSV of 60 000 $mL_{NH_3}\ g_{cat}^{-1}\ h^{-1}$ and a temperature of 450 °C over 80 h. b–d) Size distributions of Ru particles in the Ru/h-BN, Ru/Al_2O_3, and Ru/SiO_2 catalysts, respectively, before and after 80 h of reaction. The size d of the elongated Ru nanoparticle represents the distance along its long axis. The mean $\langle d \rangle$ and standard deviation σ_d of the nanoparticle size d were measured using at least 150 nanoparticles. Here, the Ru particle size in Ru/SiO_2 after the 80 h reaction is not provided because of severe sintering of the Ru particles, exceeding the plot range. e) HAADF-STEM images of Ru particles supported on h-BN after 0, 12, and 80 h of reaction. f) Adsorption energies of Ru nanoparticles composed of 60 (left), 53 (middle) and 41 (right) Ru atoms on h-BN(001) surface with varying numbers of Ru atoms at the interfaces. g) Time-series TEM images of Ru particle on h-BN sheet, observed at 450 °C under vacuum. The edge that becomes faceted over the reaction time is marked with red arrows. h) Contours of the Ru particle observed in (g) at 0 and 50 min from the onset of observation. i) H_2-TPR profiles of Ru/h-BN, Ru/Al_2O_3, and Ru/SiO_2. j) Ru 3p (left) and 3d (right) XPS profiles of unactivated and 12 h-activated Ru/h-BN catalysts. For the Ru 3p XPS spectra, the fitted peak locations of the Ru species are shown in parentheses.

Supporting Information). The observed changes in the activity strongly suggest that the morphology of the Ru active sites in the catalysts is altered during ammonia dehydrogenation. Further structural analyses are conducted to clarify the plausible morphological changes in the active sites.

The average size of the Ru nanoparticles on Al_2O_3 and SiO_2 increases considerably after 80 h, from 11.9 to 17.6 nm and from 11.7 to 25.7 nm, respectively, whereas that of Ru/h-BN mostly remains centered around 8.6 nm, as shown in Figure 2b–d and Figure S17 (Supporting Information). These results indicate that the Ru nanoparticles supported on Al_2O_3 and SiO_2 agglomerate during the ammonia decomposition reaction to reduce the surface energy.[32,33] On the other hand, the nearly identical Ru sizes of Ru/h-BN before and after the reaction suggest that the Ru nanoparticles are stabilized by h-BN. Ru nanoparticles grown heteroepitaxially on the lattice-matched h-BN surface appear to be stabilized by compressive strains, as indicated by the shift of the Ru(100) X-ray diffraction (XRD) peak in the XRD pattern (Figure S3, Supporting Information).[34] The Ru nanoparticles are further stabilized by BN overlayers that partly cover the Ru nanoparticles in the pre-activation process, preventing Ru agglomeration during the ammonia dehydrogenation (Figure S18, Supporting Information).

In addition to the strong stabilization of the Ru active sites on Ru/h-BN, the morphology of the Ru nanoparticles on h-BN changes from hexagons with rounded corners to faceted hexagons with sharpened corners as the ammonia dehydrogenation reaction proceeds, as shown in the HAADF-STEM images (Figure 2e) of the Ru/h-BN catalysts activated for different reaction times. Based on the HAADF-STEM observations (Figure 1), the straight edges of the hexagon-shaped Ru nanoparticles are the projections of the {101} planes onto the images, while the round edges are expected to be those of the higher-index facets. At elevated temperatures, the increased mobility of the surface atoms can induce the development of low-index crystal facets by removing high-index facets with higher surface energies.[35] This is supported by density functional theory (DFT) calculation results, where the most stable morphology of a Ru particle on h-BN resembles the faceted particles (Figure 2f and Experimental Section).

The development of the facets of the Ru nanoparticles at elevated temperatures is also validated by in situ TEM observation of the Ru/h-BN catalyst at 450 °C under vacuum conditions, as shown in Figure 2g (Experimental Section). The rounded edge at the bottom-left side of the Ru particle becomes straight after 50 min of annealing, as shown in Figure 2h. This indicates that the number of B_5 sites in the Ru nanoparticle increases with the annealing time, as the length of the straight edge is directly related to the length of the corresponding (001)/(101) edge. The measured total length of the straight edges of the observed Ru particle before and after the annealing is 42.06 and 49.83 nm, respectively, from which it is estimated that the number of B_5 sites in the Ru particle is ≈306 before annealing, and increases by ≈20% to ≈362 after annealing for 50 min. Note that the NH_3 conversion increases by ≈14% through the initial 50 min of preactivation, from 17.5% to 19.9% (Figure 2a). The number of the B_5 sites could increase further as the facet development proceeds with the reaction time. Notably, no agglomeration of the Ru particles is observed during the in situ TEM experiment (Figure S19, Supporting Information), indicating that the Ru nanoparticles remain stable on the h-BN surface during the high-temperature treatment.

The interactions between the Ru nanoparticles and h-BN can also contribute to the increased catalytic activity of the Ru/h-BN catalyst. To elucidate potential interactions between Ru metals and h-BN, we conducted H_2 temperature-programmed reduction (H_2-TPR) experiments. The reduction temperature of Ru/h-BN (198 °C) is higher than those of Ru/Al_2O_3 (154 °C) and Ru/SiO_2 (78 °C) (Figure 2i).The upshift of the reduction temperature peak of the Ru/h-BN catalyst indicates an enhanced metal–support interaction compared to those in the Ru/Al_2O_3 and Ru/SiO_2 catalysts.[36,37]

X-ray photoelectron spectroscopy (XPS) of Ru/h-BN shows that the binding energies of the Ru 3p and 3d levels are shifted to lower binding energies after activation for 12 h (Figure 2j and Figure S20, Supporting Information). After 12 h of the activation, Ru 3p and 3d peaks corresponding to Ru^0 in the Ru/h-BN catalysts are downshifted from 461.1 and 280.4 eV to 459.7 and 280.0 eV, respectively, as revealed by deconvolution analyses.[38] The downshift of the XPS peak for metallic Ru^0 species implies an increase in its electron density. The increased Ru electron density can be explained by the formation of defects in the h-BN during the activation, as identified by electron energy-loss spectroscopy (EELS) (Figure S21, Supporting Information).[39,40] h-BN possessing defect sites is known to undergo charge transfer from h-BN to a metal.[40,41] The observed XPS peak shift can also be caused by shape evolution of Ru nanoparticles; the Ru(101) surface, which has a relatively higher d-band center than other surfaces,[10] emerges predominantly during the shape development of the Ru nanoparticle (Figure 2e). Shifts in the Ru 3p binding energies are also observed for the Ru/Al_2O_3 and Ru/SiO_2 catalysts after the ammonia decomposition reaction (Figure S22, Supporting Information), but the shifts can come from the increase in Ru particle sizes[42] not observed for the Ru/h-BN catalyst (Figure 2b–d). The Ru^{4+} species found in the deconvoluted XPS spectra of Ru/h-BN may come from the oxidized Ru species that remain after reduction with H_2 at 450 °C.[43]

2.3. Catalytic Properties of Ru/h-BN Catalyst for Ammonia Dehydrogenation

The catalytic activity of Ru/h-BN for ammonia dehydrogenation is determined as a function of temperature, ranging from 350 to 450 °C, at a GHSV of 60 000 $mL_{NH_3}\ g_{cat}^{-1}\ h^{-1}$. The ammonia conversion increases with temperature, and the Ru/h-BN catalyst exhibits higher activity in all temperature ranges compared to the Ru/Al_2O_3 and Ru/SiO_2 catalysts (**Figure 3**a). Note that the unactivated Ru/h-BN catalyst displays higher activity than the other Ru catalysts. After 12 h of activation, the activity of the Ru/h-BN catalyst increases by approximately twofold compared to that of the unactivated Ru/h-BN. The hydrogen production rate obtained with the 12 h-activated Ru/h-BN catalyst is 1133 $mmol_{H_2}\ g_{cat}^{-1}\ h^{-1}$ at 450 °C, which is 1.6–2.2 times higher than those of the other catalysts under the same conditions, as shown in Figure 3b.

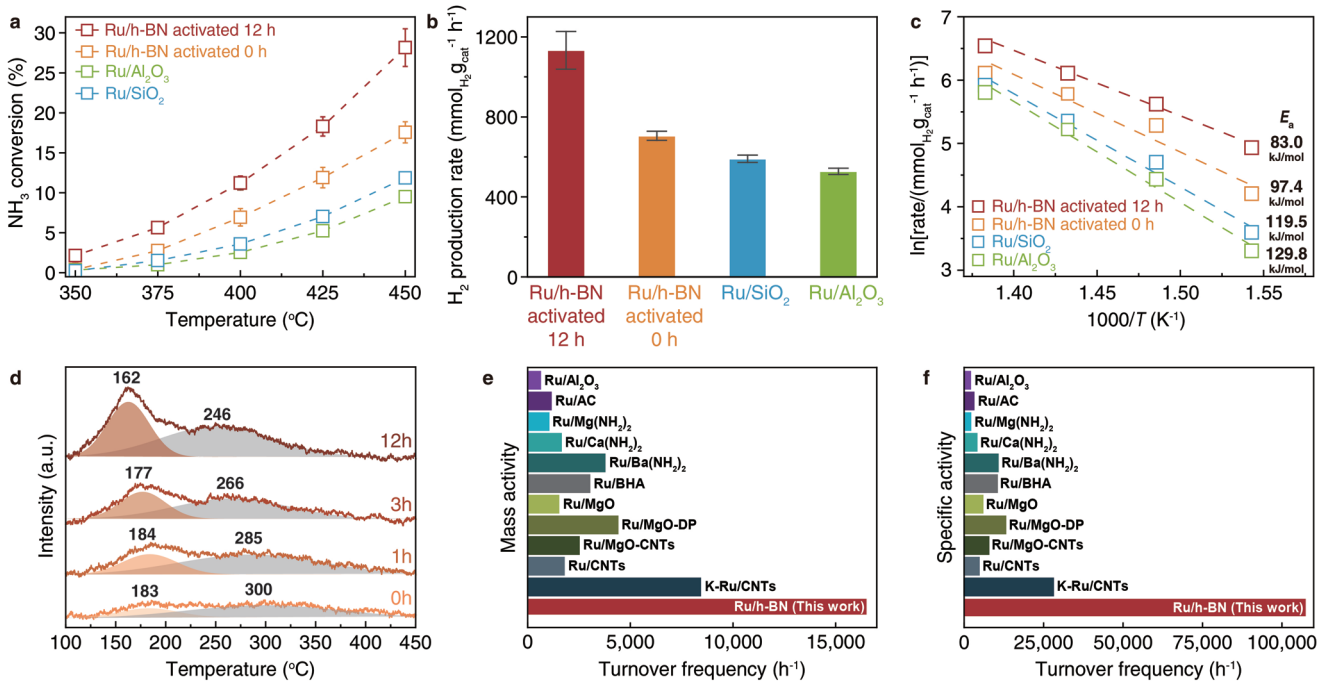

Figure 3. Evaluation of catalytic performance. a) Ammonia conversion over Ru/h-BN before activation (orange symbols), Ru/h-BN after 12 h of activation (red symbols), Ru/Al_2O_3 (green symbols), and Ru/SiO_2 (blue symbols), measured at GHSV of 60 000 mL_{NH_3} g_{cat}^{-1} h^{-1} and different temperatures (350, 375, 400, 425, and 450 °C). Error bars smaller than the symbols are omitted. b) H_2 production rates over Ru/h-BN before activation (orange), Ru/h-BN after 12 h of activation (red), Ru/Al_2O_3 (green), and Ru/SiO_2 (blue), measured at a GHSV of 60 000 mL_{NH_3} g_{cat}^{-1} h^{-1} and a temperature of 450 °C. c) Calculation of apparent activation energies of Ru/h-BN before activation (orange symbols), Ru/h-BN after 12 h of activation (red symbols), Ru/Al_2O_3 (green symbols), and Ru/SiO_2 (blue symbols) using the Arrhenius equation. d) N_2-TPD spectra of Ru/h-BN activated for different times. Desorption peaks attributed to step and terrace sites are deconvoluted and marked in red and gray, respectively. e) Mass activity and f) specific activity of Ru/h-BN for ammonia dehydrogenation, measured at a GHSV of 60 000 mL_{NH_3} g_{cat}^{-1} h^{-1} and a temperature of 450 °C, compared to those of reported catalysts.[36,44–49]

The excellent catalytic activity of the activated Ru/h-BN catalyst is attributed to the high concentration of B_5 sites in the Ru nanoparticles, which is also closely correlated with their hexagonal structures on the h-BN surface. The increased electron density of Ru in the activated Ru/h-BN catalysts also weakens the Ru—N bonds by donating electrons to the Ru—N antibonding orbitals.[7,50] These geometric and electronic effects in the Ru/h-BN catalyst facilitate the entire ammonia dehydrogenation reaction, of which the rate-determining step at low temperatures is the N_2 desorption process. Arrhenius plots for Ru/h-BN before activation, Ru/h-BN after 12 h of activation, Ru/Al_2O_3, and Ru/SiO_2 are obtained based on the hydrogen production rates measured at 375, 400, 425, and 450 °C, as illustrated in Figure 3c. The apparent activation energies of the activated Ru/h-BN and unactivated Ru/h-BN catalysts are determined to be 83.0 and 97.4 kJ mol^{-1}, respectively, lower than those obtained for other reported catalysts. The calculated apparent activation energies of Ru/Al_2O_3 and Ru/SiO_2 are 119.5 and 129.8 kJ mol^{-1}, respectively.

The promoting effect of the activated Ru/h-BN catalyst on N_2 desorption, the rate-determining step, is further elucidated by subjecting the Ru/h-BN catalysts to N_2 temperature-programmed desorption (N_2-TPD) experiments as a function of the activation time. Two distinct N_2 desorption peaks are observed regardless of the activation time, as shown in the N_2-TPD profiles in Figure 3d. Because the step sites in Ru nanoparticles have lower activation energies for N_2 desorption than the terrace sites, the TPD peaks centered at lower and higher temperatures are assigned to step and terrace sites, respectively.[10] Therefore, the ratio of the step sites to the terrace sites in the Ru/h-BN catalyst can be estimated by comparing the integrated areas under the two N_2 desorption peaks from the N_2-TPD profiles. The step/terrace ratio of the Ru species in the Ru/h-BN catalysts increases with the activation process from 0.26 to 0.61 after 12 h. This is consistent with (S)TEM observations of the Ru nanoparticles on h-BN, where the facet development of the Ru nanoparticles induces the formation of increased numbers of B_5-type step sites at the nanoparticle edges compared to the terraces. Moreover, the shifts of the N_2 desorption peaks to lower temperatures also support the promotion of N_2 desorption from both the terraces and steps of the Ru nanoparticles caused by the increased electron density. These results again support that the high activity of the Ru/h-BN catalyst originates from the selective formation of B_5 sites and the increased electron density of the Ru nanoparticles, resulting from epitaxial growth assisted by the underlying h-BN support.[10,13]

The as-synthesized Ru/h-BN catalyst exhibits superior performance for low-temperature ammonia dehydrogenation. The mass activity, the turnover frequency (TOF) per unit mass of active sites, of the 12 h-activated Ru/h-BN catalyst is determined to be 16 498 h^{-1}, which is the highest among the catalysts reported at a reaction temperature of 450 °C and a GHSV

of 60 000 $mL_{NH_3}\ g_{cat}^{-1}\ h^{-1}$, as shown in Figure 3e.[36,44–49] Specifically, the mass activity of the 12 h-activated Ru/h-BN catalyst is approximately two times higher than that of K-promoted Ru/CNT, which is well known for its high activity for ammonia dehydrogenation,[47] and ≈3.8–26.7 times higher than those of other catalysts without promoters (Table S2, Supporting Information). Moreover, the specific activity, TOF per unit number of active sites, of the 12 h-activated Ru/h-BN catalyst also demonstrates its capability to accelerate low-temperature ammonia dehydrogenation (Figure 3f).[36,44–49] The calculated specific activity (10 7481 h^{-1}) is ≈3.8–54.5 times higher than those of catalysts reported previously, under the same reaction conditions.

Depending on the morphology of Ru nanoparticles, the optimal size of Ru nanoparticles for maximizing B_5 site density can vary. For instance, it is reported that spherical Ru nanoparticles with the size of 3–4 nm achieve maximum B_5 site density.[15,18] Attempts to prepare Ru/h-BN with the Ru size of 3–4 nm were made but unsuccessful. Instead, we prepared Ru/Al_2O_3 and Ru/SiO_2 with an average size of ≈3 nm (Experimental Section and Figure S23, Supporting Information). As depicted in Figure S24 (Supporting Information), the ≈3 nm-sized Ru/SiO_2 and Ru/Al_2O_3 catalysts exhibit conversion of 19.7% and 9.22% ata GHSV 60000 $mL_{NH_3}\ g_{cat}^{-1}\ h^{-1}$ and a temperature of 450 °C respectively. The catalytic activity of the 3 nm-sized Ru/SiO_2 is comparable to that (17.5%) of the unactivated Ru/h-BN but lower than that (26.2%) of the 12 h-activated Ru/h-BN; i.e., the catalytic activity increases in the order of 10 nm-sized, 12 h-activated Ru/h-BN > 10 nm-sized, unactivated Ru/h-BN > 3 nm-sized Ru/SiO_2 > 10 nm-sized Ru/SiO_2 > 10 nm-sized Ru/Al_2O_3 ≈ 3 nm-sized Ru/Al_2O_3. Studies with HAADF-STEM show that a Ru nanoparticle with the size of ≈3 nm supported on Al_2O_3 possesses step sites on the surface (Figure S25, Supporting Information), and adatoms which occupy the step present at the edge of the Ru nanoparticle is identified. On the other hand, in the Ru/h-BN catalyst, every steps at the (101)/(001) edges of Ru nanoparticles are exposed without blocking the steps with adatoms (Figure 1g and Figure S10, Supporting Information), explaining the high activity of the Ru/h-BN catalyst toward ammonia dehydrogenation reaction.

3. Conclusion

To design a highly active and durable catalyst for low-temperature ammonia dehydrogenation, 2D h-BN with a dominant (001) facet is used as a template support to induce the formation of hexagonal planar-shaped Ru nanoparticles possessing abundant B_5 sites, which are known to exhibit high activity in ammonia dehydrogenation. Activation of the as-synthesized Ru nanoparticles at 450 °C induces a morphological change into the faceted hexagonal morphology with sharpened corners, further increasing the density of B_5 sites. The epitaxially grown activated Ru nanoparticles supported on h-BN present superior activity and stability during ammonia dehydrogenation at 450 °C. This study demonstrates that heteroepitaxy-driven morphology control plays a crucial role in selectively generating a desired nanoscale active site structure, and the synthetic route utilizing a substrate oriented by a specific facet offers a viable strategy for designing highly active heterogeneous catalysts with controlled atomic structures.

4. Experimental Section

Synthesis of the Ru/h-BN Catalyst: Ru/h-BN was prepared by the IWI with acetone as a solvent. In a typical experiment, 63.9 mg of triruthenium dodecacarbonyl (Ru_3CO_{12}, Sigma-Aldrich) dissolved in 50 mL of acetone (C_3H_6O, Samchun Pure Chemical) were used as the precursor solution. The precursor solution was added dropwise to 3 g of the dried hexagonal boron nitride power (h-BN, Alfa Aesar). The powder was shaken to distribute precursor solution, and then dried in a convection oven at 100 °C. This process was repeated until the Ru content in the catalyst reaches theoretically 1 wt%. Finally, the dried catalyst was calcined in air at 450 °C for 3 h.

Synthesis of Ru/Al_2O_3 Catalyst: The procedure for synthesizing Ru/Al_2O_3 was similar to that of Ru/h-BN. However, to match the sizes of the Ru nanoparticles in the Ru/Al_2O_3 catalyst to those of the Ru/h-BN catalyst, a ruthenium nitrosyl nitrate solution ($Ru(NO)(NO_2)_x(OH)_{3-x}$, Sigma-Aldrich) in diluted nitric acid was used to impregnate Ru in Al_2O_3 (Alfa Aesar), and the calcination was proceeded under a nitrogen flow at 300 °C for 3 h.

Synthesis of Ru/SiO_2 Catalyst: The procedure for synthesizing Ru/SiO_2 was similar to that of Ru/h-BN. However, to match the sizes of the Ru nanoparticles in the Ru/SiO_2 catalyst to those of the Ru/h-BN catalyst, a ruthenium(III) chloride hydrate ($RuCl_3{\cdot}xH_2O$, Sigma-Aldrich) solution was used to impregnate Ru in SiO_2 (Alfa Aesar), and the catalyst was calcined in the air at 300 °C for 3 h.

Synthesis of 3 nm-Sized Ru/Al_2O_3: Ru/Al_2O_3 with Ru nanoparticles with 3 nm was prepared by the IWI method with distilled water as a solvent. In a typical experiment, an aqueous solution (20 mL) containing 72.7 mg of $RuCl_3{\cdot}xH_2O$ (Sigma-Aldrich) was used as the precursor solution. The precursor solution was then added dropwise to 3.0 g of dried Al_2O_3 (Alfa Aesar). The powder was shaken gently to distribute the added precursor solution, and then dried in a convection oven at 100 °C. This process was repeated until the Ru content of the catalyst reaches theoretically 1 wt%. Finally, the dried catalyst was calcined at 800 °C for 3 h under a nitrogen flow. The Ru size of the prepared Ru/Al_2O_3 catalyst was directly measured from HAADF-STEM images, presenting the average Ru size of 3.31 nm.

Synthesis of 3 nm-Sized Ru/SiO_2: Ru/SiO_2 with Ru nanoparticles with 3 nm was prepared by the IWI method with distilled water as a solvent. In a typical experiment, an aqueous solution (20 mL) containing 72.7 mg of $RuCl_3{\cdot}xH_2O$ (Sigma-Aldrich) was used as the precursor solution. The precursor solution was then added dropwise to 3 g of dried SiO_2 (Alfa Aesar). The powder was shaken gently to distribute the added precursor solution, and then dried in a convection oven at 100 °C. This process was repeated until the Ru content of the catalyst reaches theoretically 1 wt%. Finally, the dried catalyst was calcined at 600 °C for 3 h under a nitrogen flow. The Ru size of the prepared Ru/SiO_2 catalyst was directly measured from HAADF-STEM images, presenting the average Ru size of 2.98 nm.

Adsorption/Desorption Isotherms: The nitrogen adsorption isotherms were determined using an ASAP 2000 instrument (Micrometrics) at the liquid nitrogen temperature to determine the surface area, pore volume, and pore diameter of the catalysts. Prior to the measurement, all samples were degassed in a vacuum at 250 °C for 12 h. Temperature-programmed analyses such as NH_3-TPD, CO_2-TPD, N_2-TPD, and H_2-TPR were conducted using a BELCAT-M chemisorption analyzer (MicrotracBEL Corp). Specifically, for N_2-TPD, the catalyst was first reduced in a gas flow of 75%H_2/N_2 with a flow rate of 50 mL min^{-1} at 450 °C for 30 min. If needed, the catalysts were activated in a gas flow of NH_3 with a flow rate of 40 mL min^{-1} at 450 °C for a specified time (0, 1, 3, or 12 h). Then, the gas flow was switched to N_2 gas with a flow rate of 50 mL min^{-1}, kept for 60 min at 450 °C, and cooled down to 50 °C. Once the temperature reached 50 °C, the inlet gas was replaced with He with a flow rate of

30 mL min^{-1}, and maintained for 1 h to obtain a stable baseline. The N_2-TPD was conducted by increasing the bed temperature to 450 °C at a ramp rate of 15 °C min^{-1}. The peaks of the N_2-TPD profiles presented in Figure 3d are deconvoluted using Gaussian functions with an in-house MATLAB code. The procedures for the NH_3-TPD and the CO_2-TPD were similar except for the adsorption gas. 80 mg of support was first pretreated in a He gas flow with a flow rate of 50 mL min^{-1} at 500 °C for 30 min. After that, the temperature was decreased to 100 °C, and then, the feed gas was switched to 10%NH_3/He or 10%CO_2/He gas with a flow rate of 50 mL min^{-1}. After the full adsorption of the gas species, the inlet gas was replaced with He with a flow rate of 30 mL min^{-1} at 100 °C and maintained for 1 h to obtain a stable baseline. The NH_3- or CO_2-TPD was conducted by increasing the temperature with a ramp rate of 3 °C min^{-1}. For H_2-TPR, typically, 80 mg of a catalyst was heated in a gas flow of Ar with a flow rate of 50 mL min^{-1} to 300 °C, and kept for 30 min to remove the impurities such as H_2O. After this pretreatment, the temperature of the catalyst bed was cooled down to 50 °C, and then the gas flow was replaced with 10%H_2/Ar gas at 30 mL min^{-1}. The H_2-TPR profiles were measured with a thermal conductivity detector (TCD) while the temperature increased to 500 °C at a ramp rate of 3 °C min^{-1}.

CO Chemisorption: The samples were pretreated in a He gas flow with a flow rate of 50 mL min^{-1} at 450 °C for 30 min, reduced in a H_2 gas flow with a flow rate of 50 mL min^{-1} at 450 °C for 30 min, and flushed in a He gas flow with a flow rate of 50 mL min^{-1} for 30 min to remove the adsorbed hydrogens on the catalyst surface. After this process, the temperature was decreased to 50 °C and kept for 1 h to stabilize the baseline measured in a TCD. Finally, a gas flow of 10%CO/He was introduced into the catalyst with a 0.978 mL pulse loop until saturated peaks were obtained. The number of Ru active sites per a unit mass of the catalyst was calculated by assuming that one CO molecule adsorbs to one active site of Ru.

Inductively Coupled Plasma–Optical Emission Spectroscopy (ICP-OES): Quantification of each element in the catalysts was performed using an iCAP 6000 series ICP-OES spectrometer (Thermo Scientific). ≈10 mg of the catalyst powders was digested in a 1.0 mL aqua regia solution. After the full digestion, the solution was then filtered, diluted, and analyzed in the instrument.

XPS: The surface electronic state of the catalyst was analyzed using a K-Alpha X-ray Photoelectron Spectrometer system (Thermo Scientific) with an ultrahigh-vacuum chamber using a monochromatic Al Kα radiation. The air exposure of the Ru/h-BN catalysts was reduced to less than an hour until the catalyst samples were inserted into the ultrahigh vacuum chamber of the XPS instrument. The obtained XPS spectra were calibrated by adjusting the C—C peak in the C 1s spectra to be located at 284.8 eV and fitted with Avantage Data System (Thermo Scientific).

TEM: For the all (S)TEM observations, the prepared catalysts were first reduced in a flow of 75%H_2/N_2 gas at 450 °C for 1 h, and then exposed to NH_3 gas for 0–12 h depending on the activation time. For the plan-view (S)TEM observations of the catalysts, the catalyst powders were first diluted in ethanol and sonicated. Then, a drop of the ethanol solution was placed on a lacey carbon TEM grid (SPI Supplies). For the cross-section STEM observations of the Ru/h-BN catalysts, the cross-sectional specimens were prepared by focused ion beam-scanning electron microscopy (FIB-SEM, Helios NanoLab 650, FEI Company) installed at National Center for Inter-University Research Facility (Seoul National University). First, drops of catalyst-suspended ethanol solution was placed on a Si wafer and dried under a vacuum overnight. The Si wafer with catalyst particles on its surface was coated with a thin layer of amorphous carbon with a sputter coater (208HR, Cressington), and inserted into the FIB-SEM chamber. The cross-sectional specimens were prepared by following a standard procedure where low-energy cleaning processes with a 5 and 2 kV Ga ion beam were performed to remove amorphized layers on the specimens. High-resolution TEM images of the Ru/h-BN catalysts were acquired with a JEM-ARM200F microscope (JEOL) operated at 200 kV and equipped with a cold field-emission gun, image corrector, and K3 IS camera (Gatan). Atomically resolved HAADF-STEM images and electron-energy loss spectra of the Ru/h-BN catalysts were obtained with a JEM-ARM200F microscope (JEOL) operated at 200 kV and equipped with a cold field-emission gun, probe corrector, and GIF Quantum ER spectrometer (Gatan). Both the microscopes were installed at National Center for Inter-university Research Facility (Seoul National University). The lower magnification HAADF-STEM images were acquired with a Talos F200X G2 microscope (FEI Company) operated at 200 kV, and the in situ TEM images acquired with a JEM-2100F microscope (JEOL) operated at 200 kV and a wildfire TEM holder (DENSsolution).

Catalytic Activity Test: The ammonia dehydrogenation performances of the catalysts were evaluated in a fixed-bed-flow reactor connected with a mass flow controller (F-201CB, Bronkhorst) and a multi-analog acquisition unit (PDS-1556, Pureuntek) to control the flow rate and the temperature. In a typical experiment, 40 mg of catalyst was fixed between the top and bottom quartz wools at the center of the quartz tube reactor (outer diameter 3/8 in., inner diameter 0.21 in.), and the catalyst-packed reactor was flushed with a N_2 flow for 30 min prior to the heating. The packed catalyst was heated to 450 °C at a ramp rate of 3 °C min^{-1} in a flow of 75%H_2/N_2 gas with a flow rate of 120 mL min^{-1}, kept at 450 °C for 1 h to reduce the catalyst, and then exposed to NH_3 gas with a flow rate of 40 mL min^{-1} for 0–12 h depending on the activation time. After those in situ reduction and activation processes, the catalytic activity was tested at the GHSV of 60 000 $mL_{NH_3}\ g_{cat}^{-1}\ h^{-1}$ and various temperatures (350–450 °C; see Figure 3a). The composition of the product gas was analyzed by a gas chromatography (GC)-TCD (7890A GC system equipped with CP-Volamine column, Agilent). The ammonia conversion was calculated using the following equation[9]

$$\mathrm{NH_3\ conversion}(\%) = \frac{[\mathrm{NH_3}]_{\mathrm{inlet}} - [\mathrm{NH_3}]_{\mathrm{outlet}}}{[\mathrm{NH_3}]_{\mathrm{inlet}} + [\mathrm{NH_3}]_{\mathrm{outlet}}} \times 100 \quad (1)$$

where $[NH_3]_{inlet}$ and $[NH_3]_{outlet}$ refer to the NH_3 concentrations in the reactant gas and the product gas directly measured by GC-TCD, respectively. Here, $[NH_3]_{outlet}$ considers the expansion of the product gas upon the ammonia decomposition as it is equivalent to $n_{NH_3\,outlet}/(V_{NH_3\,outlet} + V_{N_2\,outlet} + V_{H_2\,outlet})$, where $n_{NH_3\,outlet}$ denotes the number of moles of ammonia in the outlet gas, and $V_{NH_3\,outlet}$, $V_{H_2\,outlet}$, and $V_{N_2\,outlet}$ are the volumes of the unreacted ammonia, produced hydrogen, and produced nitrogen, respectively. The TOF values of the catalysts were calculated as follows

$$\mathrm{Mass\ activity}[h^{-1}] = \frac{(\mathrm{H_2\ production\ rate}) \times (\mathrm{Molecular\ weight\ of\ Ru})}{\mathrm{Ru\ contents}} \quad (2)$$

$$\mathrm{Specific\ activity}[h^{-1}] = \frac{\mathrm{Mass\ activity}[h^{-1}]}{\mathrm{Ru\ dispersion}} \quad (3)$$

where the H_2 production rate is in $mmol_{H_2}\ g_{cat}^{-1}\ h^{-1}$, the Ru contents is the percentage of Ru in a catalyst by weight, and the Ru dispersion is the ratio of the number of surface Ru atoms to that of the total Ru atoms.

DFT Calculation: Periodic DFT calculations were performed using the Vienna Ab initio Simulation Package (VASP)[51–54] with projected augmented wave (PAW)[55,56] pseudopotentials and the generalized gradient approximation (GGA) Perdew–Burke–Ernzerhof exchange-correlation functional to describe the core–valence interactions.[57] The plane-wave cutoff energy was set to 550 eV. All relaxed atom structures were fully optimized until the total energy change between self-consistent (SCF) steps was less than 10–4 eV. The Brillouin zone in reciprocal space was sampled using a Γ-centered Monkhorst–Pack scheme with 16 × 16 × 16 and 2 × 2 × 1 k-point grids for h-BN bulk and surface calculations, respectively.[58] Adsorption energies of Ru nanoparticles on the h-BN(001) surface were calculated based on the optimized structures.

Supporting Information

Supporting Information is available from the Wiley Online Library or from the author.

Acknowledgements

This work was supported by the National Research Foundation of Korea (NRF) grant funded by the Korean Government (NRF-2019M3E6A1064877 (C.W.Y. and J.P.), NRF-2017R1A5A1015365 (J.P.), NRF-2022M3I3A1082499 (C.W.Y.)) and the Institute for Basic Science (IBS-R006-D1) (J.P.). The work was also supported by the initial research grant funded by POSTECH (4.0023421.01) (C.W.Y.). J.P. acknowledges the financial support from Korea Toray Science Foundation.

Conflict of Interest

The authors declare no conflict of interest.

Author Contributions

S.K., J.C., and Y.S.J. contributed equally to this work. J.C., Y.S.J., and C.W.Y. designed the study. J.C. and Y.S.J. synthesized the catalysts and measured their activities and properties. S.K., Y.K., and C.K.S. performed TEM analysis. Y.J.L. and H.S. analyzed the supports and catalysts. D.-H.L. performed DFT calculation. S.K. and J.C. wrote the initial draft. Y.K., J.P., and C.W.Y. supervised this study. All authors contributed to the writing of the manuscript and discussion of the results.

Data Availability Statement

The data that support the findings of this study are available from the corresponding author upon reasonable request.

Keywords

ammonia dehydrogenation, B_5 site, catalysis, ruthenium, hexagonal boron nitride

Received: April 14, 2022
Revised: July 4, 2022
Published online:

[1] F. Chang, W. Gao, J. Guo, P. Chen, *Adv. Mater.* **2021**, *33*, 2005721.
[2] F. Jiao, B. Xu, *Adv. Mater.* **2019**, *31*, 1805173.
[3] J. Cha, Y. Park, B. Brigljević, B. Lee, D. Lim, T. Lee, H. Jeong, Y. Kim, H. Sohn, H. Mikulčić, K. M. Lee, D. H. Nam, K. B. Lee, H. Lim, C. W. Yoon, Y. S. Jo, *Renewable Sustainable Energy Rev.* **2021**, *152*, 111562.
[4] U. B. Demirci, P. Miele, *Energy Environ. Sci.* **2011**, *4*, 3334.
[5] F. Hayashi, Y. Toda, Y. Kanie, M. Kitano, Y. Inoue, T. Yokoyama, M. Hara, H. Hosono, *Chem. Sci.* **2013**, *4*, 3124.
[6] D. A. Hansgen, D. G. Vlachos, J. G. Chen, *Nat. Chem.* **2010**, *2*, 484.
[7] S. Mukherjee, S. V. Devaguptapu, A. Sviripa, C. R. F. Lund, G. Wu, *Appl. Catal., B* **2018**, *226*, 162.
[8] A. K. Hill, L. Torrente-Murciano, *Appl. Catal., B* **2015**, *172*, 129.
[9] P. Xie, Y. Yao, Z. Huang, Z. Liu, J. Zhang, T. Li, G. Wang, R. Shahbazian-Yassar, L. Hu, C. Wang, *Nat. Commun.* **2019**, *10*, 4011.
[10] C. A. Casey-Stevens, S. G. Lambie, C. Ruffman, E. Skúlason, A. L. Garden, *J. Phys. Chem. C* **2019**, *123*, 30458.
[11] S. Dahl, A. Logadottir, R. C. Egeberg, J. H. Larsen, I. Chorkendorff, E. Törnqvist, J. K. Nørskov, *Phys. Rev. Lett.* **1999**, *83*, 1814.
[12] S. Dahl, E. Tornqvist, I. Chorkendorff, *J. Catal.* **2000**, *192*, 381.
[13] F. R. García-García, A. Guerrero-Ruiz, I. Rodríguez-Ramos, *Top. Catal.* **2009**, *52*, 758.
[14] X. Li, W. Ji, J. Zhao, S. Wang, C. Au, *J. Catal.* **2005**, *236*, 181.
[15] J. Gavnholt, J. Schiøtz, *Phys. Rev. B: Condens. Matter Mater. Phys.* **2008**, *77*, 035404.
[16] R. L. Arevalo, S. M. Aspera, M. C. Sison Escaño, H. Nakanishi, H. Kasai, *J. Phys. Condens. Matter* **2017**, *29*, 184001.
[17] W.-Z. Li, J.-X. Liu, J. Gu, W. Zhou, S.-Y. Yao, R. Si, Y. Guo, H.-Y. Su, C.-H. Yan, W.-X. Li, Y.-W. Zhang, D. Ma, *J. Am. Chem. Soc.* **2017**, *139*, 2267.
[18] W. Rarogpilecka, E. Miskiewicz, D. Szmigiel, Z. Kowalczyk, *J. Catal.* **2005**, *231*, 11.
[19] J. Gavnholt, J. Schiøtz, *Phys. Rev. B* **2008**, *77*, 035404.
[20] A. M. Karim, V. Prasad, G. Mpourmpakis, W. W. Lonergan, A. I. Frenkel, J. G. Chen, D. G. Vlachos, *J. Am. Chem. Soc.* **2009**, *131*, 12230.
[21] M. H. Khan, H. K. Liu, X. Sun, Y. Yamauchi, Y. Bando, D. Golberg, Z. Huang, *Mater. Today* **2017**, *20*, 611.
[22] K. Aika, *Catal. Today* **2017**, *286*, 14.
[23] K. Reidy, G. Varnavides, J. D. Thomsen, A. Kumar, T. Pham, A. M. Blackburn, P. Anikeeva, P. Narang, J. M. LeBeau, F. M. Ross, *Nat. Commun.* **2021**, *12*, 1290.
[24] H. Lim, S. I. Yoon, G. Kim, A.-R. Jang, H. S. Shin, *Chem. Mater.* **2014**, *26*, 4891.
[25] Y.-R. Liu, X. Li, W.-M. Liao, A.-P. Jia, Y.-J. Wang, M.-F. Luo, J.-Q. Lu, *ACS Catal.* **2019**, *9*, 1472.
[26] J. Jones, B. Beauclair, O. Olanipekun, S. Lightbourne, M. Zhang, B. Pollok, A. Pilli, J. Kelber, *J. Vac. Sci. Technol., A* **2017**, *35*, 01B139.
[27] Z. Song, T. Cai, J. C. Hanson, J. A. Rodriguez, J. Hrbek, *J. Am. Chem. Soc.* **2004**, *126*, 8576.
[28] Y. Urashima, T. Wakabayashi, T. Masaki, Y. Terasaki, *Mineral. J.* **1974**, *7*, 438.
[29] M.-R. Li, Z. Deng, S. H. Lapidus, P. W. Stephens, C. U. Segre, M. Croft, R. P. Sena, J. Hadermann, D. Walker, M. Greenblatt, *Inorg. Chem.* **2016**, *55*, 10135.
[30] Z. Cai, B. Liu, X. Zou, H.-M. Cheng, *Chem. Rev.* **2018**, *118*, 6091.
[31] Y. Kim, S. Kang, D. Kang, K. R. Lee, C. K. Song, J. Sung, J. S. Kim, H. Lee, J. Park, J. Yi, *Angew. Chem., Int. Ed.* **2021**, *60*, 25411.
[32] A. M. Jauhar, Z. Ma, M. Xiao, G. Jiang, S. Sy, S. Li, A. Yu, Z. Chen, *J. Power Sources* **2020**, *473*, 228607.
[33] Y. Zhou, K. Neyerlin, T. S. Olson, S. Pylypenko, J. Bult, H. N. Dinh, T. Gennett, Z. Shao, R. O'Hayre, *Energy Environ. Sci.* **2010**, *3*, 1437.
[34] X. Huang, Z. Zeng, S. Bao, M. Wang, X. Qi, Z. Fan, H. Zhang, *Nat. Commun.* **2013**, *4*, 1444.
[35] M. Chi, C. Wang, Y. Lei, G. Wang, D. Li, K. L. More, A. Lupini, L. F. Allard, N. M. Markovic, V. R. Stamenkovic, *Nat. Commun.* **2015**, *6*, 8925.
[36] X. Ju, L. Liu, P. Yu, J. Guo, X. Zhang, T. He, G. Wu, P. Chen, *Appl. Catal., B* **2017**, *211*, 167.
[37] X. Li, X. Yang, Y. Huang, T. Zhang, B. Liu, *Adv. Mater.* **2019**, *31*, 1902031.
[38] D. J. Morgan, *Surf. Interface Anal.* **2015**, *47*, 1072.
[39] O. Cretu, Y.-C. Lin, M. Koshino, L. H. G. Tizei, Z. Liu, K. Suenaga, *Phys. Rev. Lett.* **2015**, *114*, 075502.
[40] W. Zhu, Z. Wu, G. S. Foo, X. Gao, M. Zhou, B. Liu, G. M. Veith, P. Wu, K. L. Browning, H. N. Lee, H. Li, S. Dai, H. Zhu, *Nat. Commun.* **2017**, *8*, 15291.
[41] S. A. Aal, *Surf. Sci.* **2016**, *644*, 1.
[42] H. Wang, X.-K. Gu, X. Zheng, H. Pan, J. Zhu, S. Chen, L. Cao, W.-X. Li, J. Lu, *Sci. Adv.* **2019**, *5*, eaat6413.
[43] V. Mazzieri, *Appl. Surf. Sci.* **2003**, *210*, 222.
[44] S.-F. Yin, B.-Q. Xu, C.-F. Ng, C.-T. Au, *Appl. Catal., B* **2004**, *48*, 237.
[45] P. Yu, J. Guo, L. Liu, P. Wang, F. Chang, H. Wang, X. Ju, P. Chen, *J. Phys. Chem. C* **2016**, *120*, 2822.
[46] G. Li, M. Kanezashi, T. Tsuru, *Catalysts* **2017**, *7*, 23.

[47] S. J. Wang, S. F. Yin, L. Li, B. Q. Xu, C. F. Ng, C. T. Au, *Appl. Catal., B* **2004**, *52*, 287.
[48] S. F. Yin, B. Q. Xu, S. J. Wang, C. F. Ng, C. T. Au, *Catal. Lett.* **2004**, *96*, 113.
[49] Z. Wang, Z. Cai, Z. Wei, *ACS Sustainable Chem. Eng.* **2019**, *7*, 8226.
[50] J. Cha, T. Lee, Y.-J. Lee, H. Jeong, Y. S. Jo, Y. Kim, S. W. Nam, J. Han, K. B. Lee, C. W. Yoon, H. Sohn, *Appl. Catal., B* **2021**, *283*, 119627.
[51] G. Kresse, J. Furthmüller, *Phys. Rev. B* **1996**, *54*, 11169.
[52] G. Kresse, J. Hafner, *Phys. Rev. B* **1994**, *49*, 14251.
[53] G. Kresse, J. Hafner, *Phys. Rev. B* **1993**, *47*, 558.
[54] G. Kresse, J. Furthmüller, *Comput. Mater. Sci.* **1996**, *6*, 15.
[55] P. E. Blöchl, *Phys. Rev. B* **1994**, *50*, 17953.
[56] G. Kresse, D. Joubert, *Phys. Rev. B* **1999**, *59*, 1758.
[57] J. P. Perdew, K. Burke, M. Ernzerhof, *Phys. Rev. Lett.* **1996**, *77*, 3865.
[58] H. J. Monkhorst, J. D. Pack, *Phys. Rev. B* **1976**, *13*, 5188.